

Linear-scaling source-sink algorithm for simulating time-resolved quantum transport and superconductivity

Joseph Weston and Xavier Waintal

*Université Grenoble Alpes, INAC-SPSMS, F-38000 Grenoble, France
and CEA, INAC-SPSMS, F-38000 Grenoble, France*

(Received 29 October 2015; revised manuscript received 22 March 2016; published 14 April 2016)

We report on a “source-sink” algorithm which allows one to calculate time-resolved physical quantities from a general nanoelectronic quantum system (described by an arbitrary time-dependent quadratic Hamiltonian) connected to infinite electrodes. Although mathematically equivalent to the nonequilibrium Green’s function formalism, the approach is based on the scattering wave functions of the system. It amounts to solving a set of generalized Schrödinger equations that include an additional “source” term (coming from the time-dependent perturbation) and an absorbing “sink” term (the electrodes). The algorithm execution time scales linearly with both system size and simulation time, allowing one to simulate large systems (currently around 10^6 degrees of freedom) and/or large times (currently around 10^5 times the smallest time scale of the system). As an application we calculate the current-voltage characteristics of a Josephson junction for both short and long junctions, and recover the multiple Andreev reflection physics. We also discuss two intrinsically time-dependent situations: the relaxation time of a Josephson junction after a quench of the voltage bias, and the propagation of voltage pulses through a Josephson junction. In the case of a ballistic, long Josephson junction, we predict that a fast voltage pulse creates an oscillatory current whose frequency is controlled by the Thouless energy of the normal part. A similar effect is found for short junctions; a voltage pulse produces an oscillating current which, in the absence of electromagnetic environment, does not relax.

DOI: [10.1103/PhysRevB.93.134506](https://doi.org/10.1103/PhysRevB.93.134506)

I. INTRODUCTION

As quantum nanoelectronics experiments get faster (in the GHz range and above) it becomes possible to study the time-dependent dynamics of devices in their quantum regimes, i.e., at frequencies higher than the system temperature (1 K corresponds roughly to 20 GHz). Recent achievements include coherent single electron sources with a well-defined release time [1] or energy [2], pulse propagation along quantum Hall edge states [3–5], and terahertz measurements in carbon nanotubes [6]. While the mathematical framework for describing quantum transport in the time domain has been around since the 1990’s [7,8], a direct integration of the corresponding nonequilibrium Green’s functions (NEGFs) is rather cumbersome, even for noninteracting systems—the focus of this paper—and can only be solved either in restricted contexts [9–11], or with the help of numerics that scale polynomially with the number of degrees of freedom/required simulation time [12–16]. A large effort was made by the community to come up with more efficient algorithms within the NEGF or equivalent wave function formalism [17–20]. In particular, the approach of Ref. [21] (to which the present paper is a sequel) was recently used in a variety of situations, including electronic interferometers [22,23], quantum Hall effect [24], normal-superconducting junctions [25], Floquet topological insulators [26], and the calculation of the quantum noise of voltage pulses [27].

The best algorithm introduced in Ref. [21] (nicknamed WF-C) has a computational execution time that scales linearly with the system size N , but as the square of the total simulation time. While for ballistic systems this t_{\max}^2 limitation was not too stringent, in situations with large separations of time scales (such as the Josephson junctions studied below), it makes numerical calculations computationally prohibitive. In this paper, we present an extension of the previous approach

that reduces the computational complexity down to $O(Nt_{\max})$. This is achieved with the addition of non-Hermitian terms, referred to as “sink” terms, in the Hamiltonian, in addition to the “source” terms introduced in the WF-C method of Ref. [21]. This technique remains mathematically equivalent to the NEGF formalism.

This article is organized as follows. Section II introduces a general class of models and the time-dependent scattering states of the system. In Sec. III we briefly recall how a simple change of variables leads to the introduction of an additional source term in the Schrödinger equation, which greatly facilitates the numerical treatment. In Sec. IV we develop the new part of the algorithm and show how the introduction of sink terms solves previous difficulties at long times. Finally, Sec. V discusses applications to the physics of out of equilibrium Josephson junctions. After recovering well-known effects [multiple Andreev reflection (MAR) in both short and long junctions, ac Josephson effect, relaxation of Andreev bound states], we study the propagation of fast voltage pulses through Josephson junctions.

II. MODEL

We consider a general class of models describing a quantum device of finite extent attached to semi-infinite electrodes. The full system is described by a general quadratic Hamiltonian of the form

$$\hat{H}(t) = \sum_{ij} H_{ij}(t) \hat{c}_i^\dagger \hat{c}_j, \quad (1)$$

where \hat{c}_i^\dagger (\hat{c}_j) are the fermionic creation (annihilation) operators of a one-particle state on site i (j). A “site” i typically labels position as well as other degrees of freedom such as spin, orbital angular momentum, or electron/hole (as in the superconducting application below). The $H_{ij}(t)$ are the matrix

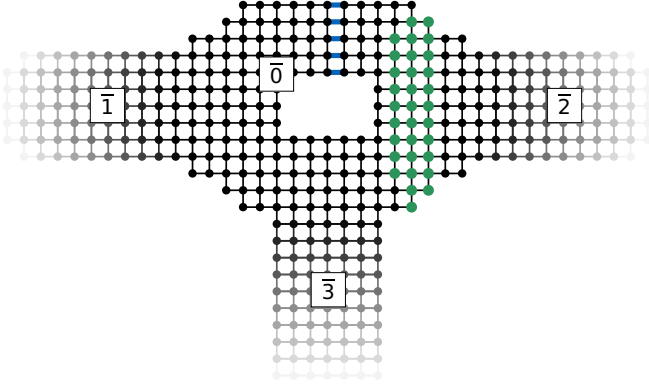


FIG. 1. Sketch of a typical system considered. It consists of a central scattering region $\bar{0}$ attached to semi-infinite leads $\bar{1}$, $\bar{2}$, and $\bar{3}$. Some of the on-site potentials are time dependent (for instance, the bold green sites correspond to the sites underneath a pulsed electrostatic gate) as well as some of the intersite hoppings (for instance, the blue connections correspond to a time-dependent magnetic field sent through the central hole).

elements of the Hamiltonian matrix $\mathbf{H}(t)$. The system consists of a time-dependent central region $\bar{0}$ connected to several leads $\bar{1}, \bar{2}, \dots$, as depicted in Fig. 1. We keep the Hamiltonian of the central region fully general but restrict the leads to be semi-infinite, time independent, and invariant by translation (i.e., they have a quasi-one-dimensional periodic structure). Each lead remains in its thermal equilibrium at all times. We further suppose that the time-dependent perturbations are only switched on at positive times, so that $\mathbf{H}(t < 0) = \mathbf{H}_0$. Note that if one has a uniform time-varying potential in one or more of the leads, then a gauge transformation can always be performed such that the time dependence is brought into the interface between the lead and the central region, which can then be included in the definition of the central region. Typically the time-dependent part of the Hamiltonian is restricted to rather small regions, as illustrated in Fig. 1.

Before the time-dependent perturbations are switched on, the system is characterized by its scattering wave functions $\Psi_{\alpha E}^{\text{st}}$ that are labeled by their energy E and incoming channel α ,

$$\mathbf{H}_0 \Psi_{\alpha E}^{\text{st}} = E \Psi_{\alpha E}^{\text{st}}. \quad (2)$$

The scattering states $\Psi_{\alpha E}^{\text{st}}$ are standard objects of mesoscopic physics and can be obtained directly by wave matching the incoming and outgoing modes at the lead-system boundary. For complicated geometries these can be obtained numerically by using, e.g., the KWANT package [28]. A physical observable $\hat{A} = \sum_{ij} A_{ij} \hat{c}_i^\dagger \hat{c}_j$ (e.g., electronic density or local currents) can be directly obtained from the knowledge of these wave functions by simply filling up the one-body scattering states according to Fermi statistics, using

$$\langle \hat{A} \rangle = \sum_{\alpha} \int \frac{dE}{2\pi} f_{\alpha}(E) \Psi_{\alpha E}^{\text{st}\dagger} \mathbf{A} \Psi_{\alpha E}^{\text{st}}, \quad (3)$$

where $f_{\alpha}(E)$ is the Fermi function of the electrode associated with channel α . The celebrated Landauer formula for the conductance is a special case of Eq. (3).

The generalization of Eq. (3) to the time-dependent problem is rather straightforward: One first obtains the scattering states and lets them evolve according to the Schrödinger equation

$$i \partial_t \Psi_{\alpha E}(t) = \mathbf{H}(t) \Psi_{\alpha E}(t), \quad (4)$$

with the initial condition $\Psi_{\alpha E}(t = 0) = \Psi_{\alpha E}^{\text{st}}$. The observables follow from Eq. (3) where the $\Psi_{\alpha E}^{\text{st}}$ are replaced by $\Psi_{\alpha E}(t)$:

$$\langle \hat{A}(t) \rangle = \sum_{\alpha} \int \frac{dE}{2\pi} f_{\alpha}(E) \Psi_{\alpha E}^{\dagger}(t) \mathbf{A} \Psi_{\alpha E}(t). \quad (5)$$

The fact that such a scheme is equivalent to the NEGF formalism, or to the scattering approach, was derived in Ref. [21]. In particular, the central objects of the NEGF formalism, the so-called lesser ($<$), greater ($>$), and retarded (R) Green's functions, have simple expressions in terms of the time-dependent scattering states,

$$G_{ij}^{<}(t, t') \equiv i \langle \hat{c}_j^{\dagger}(t') \hat{c}_i(t) \rangle = \sum_{\alpha} \int \frac{dE}{2\pi} i f_{\alpha}(E) \Psi_{\alpha E}(t, i) \Psi_{\alpha E}^*(t', j), \quad (6)$$

$$G_{ij}^{>}(t, t') \equiv -i \langle \hat{c}_i(t) \hat{c}_j^{\dagger}(t') \rangle = \sum_{\alpha} \int \frac{dE}{2\pi} i [f_{\alpha}(E) - 1] \Psi_{\alpha E}(t, i) \Psi_{\alpha E}^*(t', j), \quad (7)$$

$$G_{ij}^R(t, t') \equiv -i \theta(t - t') \langle \hat{c}_j^{\dagger}(t') \hat{c}_i(t) + \hat{c}_i(t) \hat{c}_j^{\dagger}(t') \rangle = -i \theta(t - t') \sum_{\alpha} \int \frac{dE}{2\pi} \Psi_{\alpha E}(t, i) \Psi_{\alpha E}^*(t', j). \quad (8)$$

Note that in the presence of bound states (such as the Andreev states in the Josephson junctions described below) the above integral needs to be replaced by an integral over the continuum plus a sum over the bound states, as explained in Ref. [29].

III. THE SOURCE

In its original form, Eq. (4) is not very useful for numerics because the wave function spreads over the entire *infinite* system. A first simple, yet crucial, step consists of introducing the deviation $\bar{\Psi}_{\alpha E}(t)$ from the stationary solution:

$$\Psi_{\alpha E}(t) = e^{-iEt} [\Psi_{\alpha E}^{\text{st}} + \bar{\Psi}_{\alpha E}(t)]. \quad (9)$$

$\bar{\Psi}_{\alpha E}(t)$ satisfies

$$i \partial_t \bar{\Psi}_{\alpha E}(t) = [\mathbf{H}(t) - E] \bar{\Psi}_{\alpha E}(t) + S_{\alpha E}(t), \quad (10)$$

with

$$S_{\alpha E}(t) = [\mathbf{H}(t) - \mathbf{H}_0] \Psi_{\alpha E}^{\text{st}} \quad (11)$$

and

$$\bar{\Psi}_{\alpha E}(t = 0) = 0. \quad (12)$$

The new “source” term $S_{\alpha E}(t)$ can be computed from the knowledge of the stationary scattering states and is localized at the place where the time-dependent perturbation takes place [where $\mathbf{H}(t) \neq \mathbf{H}_0$, typically the colored regions of Fig. 1]. Equation (10) is already much better than Eq. (4) for numerics because the initial condition corresponds to a wave function that vanishes everywhere. One can therefore truncate Eq. (10)

and keep a finite system around the central time-dependent region where the source term lies. In practice, one adds N layers of each electrode. Note that in order for this procedure to be correct, the stationary scattering states are calculated for the *infinite* system and the truncation is only performed afterwards. For the truncation to be valid, the size of this finite region must be larger than $N > v t_{\max}/2$, where v is the maximum group velocity at which the wave function can propagate and t_{\max} the duration of the simulation. Hence, for large values of t_{\max} , the total computational time to integrate Eq. (4) scales as $v t_{\max}^2$. This algorithm corresponds to the WF-C algorithm of Ref. [21]. In Sec. IV we will see that we can go beyond the WF-C method by introducing a complex absorbing potential in the region of added electrode. This will allow us to obtain the promised linear scaling.

The keen reader will notice that we have actually removed a factor e^{-iEt} from the definition of $\tilde{\Psi}_{\alpha E}(t)$ compared to the WF-C method of Ref. [21]. This change, while small, leads to an improved stability of the numerical integration: The equation of motion for $\tilde{\Psi}_{\alpha E}(t)$ does not have an (potentially fast) oscillating factor e^{-iEt} in the source term. This means that the numerical integration scheme used for solving Eq. (10) is now limited by the intrinsic time scales of the problem, and not the “artificial” time scale \hbar/E introduced by a bad choice of gauge.

IV. THE SINK

The t_{\max}^2 scaling of the algorithm comes from the fact that for long simulation times, one needs to introduce a large part of the leads ($\propto t_{\max}$) in order to avoid spurious reflections at the boundaries where the leads have been truncated. To proceed, one needs to take advantage of the special structure of the leads: They are not only time independent, but also invariant by translation. Hence, whatever enters into the lead will propagate towards infinity and never come back to the central region. Mathematically, the form of $\tilde{\Psi}_{\alpha E}(t)$ in the leads is a superposition of *outgoing* plane waves [21]

$$\tilde{\Psi}_{\alpha E}(t) = \sum_{\alpha'} \int \frac{dE'}{2\pi} S_{\alpha'\alpha}(E', E) e^{-iE't + k'n} \xi_{\alpha'}(E'), \quad (13)$$

where E' and k' are related by the dispersion relation of the lead, n indexes the different unit cells in the lead, $\xi_{\alpha'}$ the transverse wave function of the corresponding mode, and $S_{\alpha'\alpha}(E', E)$ is the time-dependent part of the inelastic scattering matrix. The crucial point of Eq. (13) is that it only contains outgoing modes, as the incoming one has been subtracted when removing the stationary scattering state. Therefore, once the wave function starts to reach the leads, it propagates toward infinity and never comes back to the central system.

A natural idea that comes to mind is to replace the finite fraction of the electrodes by some sort of (non-Hermitian) term in the Hamiltonian that “absorbs” the wave function that enters the leads. This has been studied in the literature in the context of various partial differential equations [30–38], and is usually known as a complex absorbing potential. The difficulty lies in the fact that this absorbing term must not give rise to reflections. At a given energy, a perfectly absorbing boundary condition does exist, it corresponds to adding the self-energy

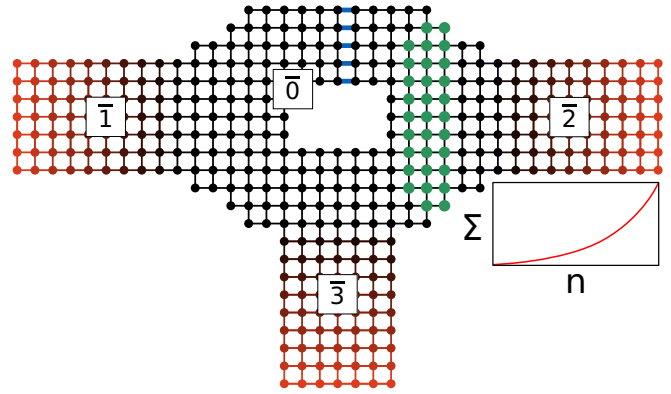


FIG. 2. Sketch of the truncated approximation to the system shown in Fig. 1, including the absorbing layers. The (red) color of the sites indicates the intensity of the complex absorbing potential. The curve next to lead 2’s absorbing layer shows a typical shape of the complex absorbing potential Σ .

of the lead at the boundary (which is a nonlocal complex absorbing potential; see the WF-D method of Ref. [21]). However, the outgoing waves of Eq. (13) span a finite energy window so that some energies would get reflected back to the central region. One solution to obtain a perfectly absorbing boundary condition is to use a boundary condition that is nonlocal in time [30], as in the WF-B method of Ref. [21]; this leads to algorithms that scale as t_{\max}^2 .

We choose instead to design an imaginary potential that varies spatially. We show that *for any desired accuracy*, we can design an imaginary potential that spreads over a finite width of N electrode unit cells—where N depends only on the required accuracy, not on t_{\max} . In practice, this algorithm is much more effective than WF-C when t_{\max} becomes larger than the ballistic time of flight through the system. The idea behind the algorithm is fairly straightforward: Suppose that a plane wave with a dispersion relation $E(k)$ propagates inside one electrode. If one adds an imaginary potential $-i\Sigma$ to the Schrödinger equation, this plane wave becomes evanescent, which eventually leads to the absorption of the wave. On the other hand, any abrupt variation of the potential (or in this case of imaginary potential) leads to unwanted reflection back to the central part of the system. Hence, the algorithm consists of adiabatically switching on the imaginary potential $\Sigma(n)$ inside a finite fraction of the electrode (see Fig. 2 for a sketch). This equation of motion contains both the previous source term and the additional sink in the electrodes,

$$i \partial_t \tilde{\Psi}_{\alpha E}(t) = [\mathbf{H}(t) - E - i \Sigma] \tilde{\Psi}_{\alpha E}(t) + S_{\alpha E}(t), \quad (14)$$

where the matrix Σ is diagonal and vanishes in the central region while it reads

$$\Sigma = \Sigma(n) \mathbf{1}_{\text{cell}} \quad (15)$$

in the absorbing layer placed at the beginning of the electrodes. The index n labels the unit cells of the leads and $\mathbf{1}_{\text{cell}}$ is the identity matrix defined over a unit cell. What remains to be done is to specify the function $\Sigma(n)$ so that it is large enough to absorb all waves entering into the lead while being smooth enough not to produce spurious reflections. The error induced by the boundary conditions must not exceed a tolerance δ . Our

aim is to minimize the number N of layers that must be added in the simulation to absorb the outgoing waves without the error exceeding δ .

A. Analytical calculation of the spurious reflection

Before we can design a suitable imaginary potential, we must understand how the spurious reflection back to the central part depends on the shape of $\Sigma(n)$. We will start from a continuum model in order to develop an analytical solution for this simple case. The rationale, other than its tractability, is the fact that spurious reflections happen when $\Sigma(n)$ varies on a spatial scale that is short *compared to the wavelength* of the solution, hence it is dominated by small momentum k where the tight-binding dispersion relation reduces to its continuum limit. We will show that there is an extremely good agreement between the analytical results derived in this section and numerical calculations of the discretized model.

Let us consider the stationary one-dimensional (1D) Schrödinger equation,

$$-\frac{\hbar^2}{2m^*} \frac{\partial^2 \psi(x)}{\partial x^2} - \frac{i}{L} \Sigma\left(\frac{x}{L}\right) \psi(x) = E \psi(x), \quad (16)$$

where m^* is the electron effective mass and we have introduced a length scale L , which controls how fast $\Sigma(x)$ varies. For negative x , we set $\Sigma(x \leq 0) = 0$ so that the wave function is in a superposition of plane waves,

$$\psi(x) = e^{ikx} + r_\Sigma e^{-ikx}, \quad (17)$$

where we *define* $E = \hbar^2 k^2 / 2m^*$. Our goal is to calculate the spurious reflection probability $R_\Sigma = |r_\Sigma|^2$ induced by the presence of the imaginary potential. We first rescale the equation by E and define $\bar{x} = kx$, $\bar{\Sigma}(u) = (k/E)\Sigma(u)$, and $\psi(x) = \bar{\psi}(\bar{x})$ to obtain the dimensionless equation

$$\left[\partial_{\bar{x}}^2 + \frac{i}{kL} \bar{\Sigma}\left(\frac{\bar{x}}{kL}\right) + 1 \right] \bar{\psi}(\bar{x}) = 0, \quad (18)$$

with

$$\bar{\psi}(\bar{x}) = e^{i\bar{x}} + r_\Sigma e^{-i\bar{x}} \quad (19)$$

for $\bar{x} < 0$. It is apparent from Eq. (18) that the spurious reflection is controlled by the dimensionless parameter kL . Since we want this spurious reflection to be small, we will work in the limit of large $kL \gg 1$ and expand r_Σ in powers of $1/kL$. The zeroth-order contribution is simply the extension of the WKB limit to imaginary potential; the wave function takes the form of an evanescent wave,

$$\bar{\psi}(\bar{x}) \approx e^{\bar{S}(\bar{x})}, \quad (20)$$

with $\bar{S}(\bar{x})$ satisfying

$$[\bar{S}'(\bar{x})]^2 + 1 + i \frac{1}{kL} \bar{\Sigma}\left(\frac{\bar{x}}{kL}\right) = 0, \quad (21)$$

where the primes denote derivatives. We expand $\bar{S}(\bar{x})$ to first order in $1/kL$, and apply the boundary condition Eq. (19) at $\bar{x} = 0$, as well as $\bar{\psi}(kL) = 0$ (perfect reflection at the end of the simulation domain at $x = L$) to obtain the zeroth-order contribution to r_Σ ,

$$r_\Sigma^0 = e^{2ikL} e^{-Ak/E}, \quad (22)$$

where

$$A = \int_0^L \frac{1}{L} \Sigma\left(\frac{x}{L}\right) dx \quad (23)$$

is independent of kL . Physically speaking, the wave function is exponentially attenuated up to the hard wall at $x = L$ where it is fully reflected and then again exponentially attenuated until $x = 0$.

The contribution r_Σ^0 takes into account the finite absorption due to the imaginary potential, but not the spurious reflections due to wave-vector mismatch. It is therefore necessary to go beyond the *adiabatic* WKB approximation and calculate its $1/kL$ deviation r_Σ^1 . We can ignore the hard wall at $x = L$ as it will play no role in what follows. Generalizing the WKB approximation we choose the following ansatz for $\bar{x} > 0$:

$$\bar{\psi}(\bar{x}) = \bar{\phi}(\bar{x}) e^{\bar{S}(\bar{x})}. \quad (24)$$

$\bar{S}(\bar{x})$ contains the fast oscillating and decaying parts, while $\bar{\phi}(\bar{x})$ contains the remaining (slow) parts. Plugging the ansatz Eq. (24) into Eq. (18), our Schrödinger equation becomes

$$\left\{ \bar{\phi}''(\bar{x}) + \left[2i - \frac{1}{kL} \bar{\Sigma}\left(\frac{\bar{x}}{kL}\right) + 2O\left(\frac{1}{(kL)^2}\right) \right] \bar{\phi}'(\bar{x}) + \left[\frac{-1}{2(kL)^2} \bar{\Sigma}'\left(\frac{\bar{x}}{kL}\right) + O\left(\frac{1}{(kL)^3}\right) \right] \bar{\phi}(\bar{x}) \right\} e^{\bar{S}(\bar{x})} = 0, \quad (25)$$

with

$$\bar{S}(\bar{x}) = i\bar{x} - \frac{1}{2} \int_0^{\bar{x}/kL} \bar{\Sigma}(u) du + O\left(\frac{1}{kL}\right). \quad (26)$$

We write $\bar{\phi}(\bar{x})$ as $\bar{\phi}(\bar{x}) = \bar{\phi}_0(\bar{x}) + (1/kL)\bar{\phi}_1(\bar{x})$ and notice that, in the limit $(1/kL) \rightarrow 0$, Eq. (25) admits a solution $\bar{\phi}(\bar{x}) = \bar{\phi}_0(\bar{x}) = A + B e^{-2i\bar{x}}$. In this limit there should be no backscattering from the imaginary potential, so $B = 0$ and $\bar{\phi}_0(\bar{x}) = 1$, to match the boundary conditions Eq. (19). The derivatives of $\bar{\phi}_0(\bar{x})$ hence vanish and we arrive at

$$\bar{\phi}_1''(\bar{x}) + 2 \left[i - \frac{1}{2kL} \bar{\Sigma}(\bar{x}/kL) \right] \bar{\phi}_1'(\bar{x}) = \frac{1}{2kL} \bar{\Sigma}'(\bar{x}/kL) \quad (27)$$

up to terms of order $O([1/kL]^2)$. Equation (27) can be solved by the variation of constant method,

$$\bar{\phi}_1'(\bar{x}) = \bar{C}(\bar{x}) \exp \left[-2i\bar{x} + \int_0^{\bar{x}/kL} \bar{\Sigma}(u) du \right], \quad (28)$$

with

$$\bar{C}'(\bar{x}) = \frac{1}{2kL} \bar{\Sigma}'(\bar{x}/kL) \exp \left[2i\bar{x} - \int_0^{\bar{x}/kL} \bar{\Sigma}(u) du \right]. \quad (29)$$

Applying the continuity condition on $\bar{\psi}(\bar{x})$ and $\bar{\psi}'(\bar{x})$ at $\bar{x} = 0$ we obtain the first-order contribution to the reflection amplitude,

$$r_\Sigma^1 = \frac{-1}{2ikL} \bar{C}(0), \quad (30)$$

which we can write explicitly, using Eq. (29) and the condition $\bar{C}(\infty) = 0$, as

$$r_{\Sigma}^1 = \frac{1}{4ikL} \int_0^{\infty} \bar{\Sigma}'(u) \exp \left[2ikLu - \int_0^u \bar{\Sigma}(v)dv \right] du. \quad (31)$$

One can understand r_{Σ}^1 as the Fourier transform at (large) frequency (kL) of the gradient of the imaginary potential weighted by the absorption that has already taken place. Putting together Eqs. (22) and (31), we finally obtain

$$r_{\Sigma} = e^{2ikL} e^{-Ak/E} + \frac{1}{4iEL} \int_0^{\infty} \Sigma'(u) \times \exp \left[2ikLu - \frac{k}{E} \int_0^u \Sigma(v)dv \right] du. \quad (32)$$

Equation (32) is the main result of this section. Now that we understand how the spurious reflection depends on the shape of $\Sigma(x)$, we need to design the imaginary potential so as to minimize Eq. (32) (for a given L). More precisely, for a given required precision ϵ , we wish to enforce $R_{\Sigma} < \epsilon$ irrespective of the value of the energy E . Such a stringent condition is not, strictly speaking, feasible as $R_{\Sigma} \rightarrow 1$ when $E \rightarrow 0$ (all the variations of the imaginary potential become ‘‘abrupt’’ when the electronic wavelength becomes infinite), but we will see that the associated error can be kept under control.

For a fixed L and A we wish to choose a form for $\Sigma(x)$ that will minimize the reflection at all energies. We leave a full optimization of this shape for future study and focus on an algebraic one,

$$\Sigma(u) = (n+1)Au^n, \quad (33)$$

from which the reflection amplitude calculated from Eq. (32) reads

$$r_{\Sigma} = e^{2ikL} e^{-Ak/E} + \frac{An(n+1)(n-1)}{2^{n+2}Ek^n L^{n+1}}. \quad (34)$$

As a consistency check of the approach developed above, we compare this analytical result for the reflection probability with direct numerical calculation using the KWANT dc transport package [28]. To do so we discretize the continuous Schrödinger equation onto a lattice of lattice spacing 1. Figure 3 shows how R_{Σ} scales for the case $n = 2$ and $n = 6$, showing an excellent agreement between the direct numerical simulations and the above analytical result in the limit of validity of the latter (small reflection). Figure 3(c) shows

that the reflection has a minimum as a function of A which corresponds to a compromise between the first and last term of Eq. (34). Once A has been chosen large enough for the first term of Eq. (34) to be negligible, one can always choose L large enough to control the second term. We can already anticipate that the difficulties will come from vanishing energies $E \rightarrow 0$ for which the spurious reflection goes toward unity.

B. Numerical precision in the time domain

Now that we understand the dc case, let us consider the previous one-dimensional model in the time domain and send a Gaussian voltage pulse through the wire. This problem has been studied in detailed in Ref. [21], to which we refer for more details. We compute the current flowing and measure the error with respect to a reference calculation $I_E^{\text{ref}}(t)$,

$$\delta = \frac{\int_0^{t_{\text{max}}} |I_E(t) - I_E^{\text{ref}}(t)| dt}{\int_0^T |I_E^{\text{ref}}(t)| dt}, \quad (35)$$

where $I_E(t)$ is the time-dependent probability current for a particle injected at energy E using the above-designed imaginary potential to absorb the outgoing waves. The reference calculation is performed without an imaginary potential, but with enough added unit cells in the leads such that the solution does not have time to propagate back into the central region before the end of the simulation; this corresponds to the WF-C method of Ref. [21].

Figure 4(a) shows the scaling of the error δ in the time-dependent calculation with respect to the dc reflection probability of the absorbing region R_{Σ} as L is changed. The current at an energy at the center of the spectrum is calculated. We see from Fig. 4 that for very short absorbing regions the error scales proportionally to R_{Σ} , whereas for longer regions it scales as $\sqrt{R_{\Sigma}}$. This simply reflects the fact that the error on $\Psi_{\alpha E}(t)$ is proportional to $\sqrt{R_{\Sigma}} = r_{\Sigma}$: Since the current (hence δ) is quadratic in $\Psi_{\alpha E}(t) \equiv e^{-iEt} [\Psi_{\alpha E}^{\text{st}} + \bar{\Psi}_{\alpha E}(t)]$, the error has the form $\delta \sim 2|\Psi_{\alpha E}^{\text{st}}| \sqrt{R_{\Sigma} + R_{\Sigma}}$. More importantly, we see that we can control the error of the calculation with arbitrary precision and for extremely long times (we checked this last point for much longer times than those shown in the inset).

More interesting is the behavior of the error δ as a function of the injection energy E . Indeed, since there are large spurious reflections when $E \rightarrow 0$, we might expect δ to behave badly

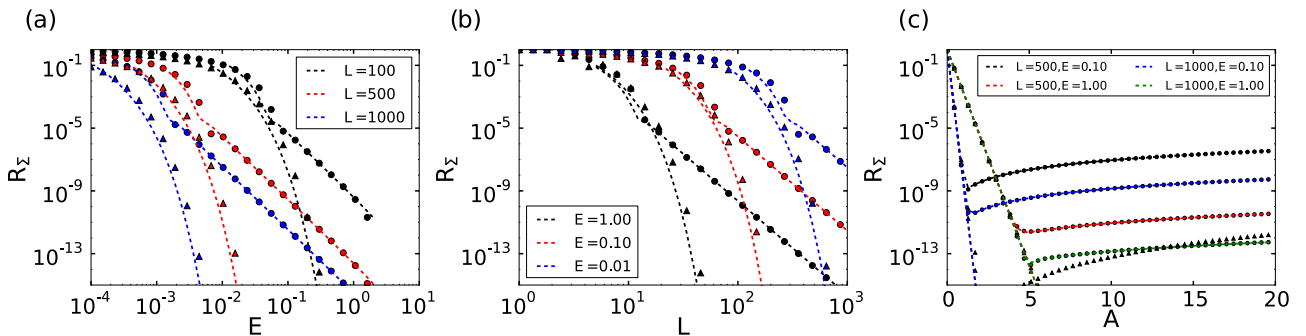


FIG. 3. dc reflection probability of a one-dimensional chain in presence of an imaginary potential. The three panels show the scaling with (a) energy, (b) absorbing region length, and (c) area under the imaginary potential curve. Symbols are the numerical simulation of the discrete model and dashed lines are the analytic (continuum) result, Eq. (34), with $n = 2$ (circles) and $n = 6$ (triangles).

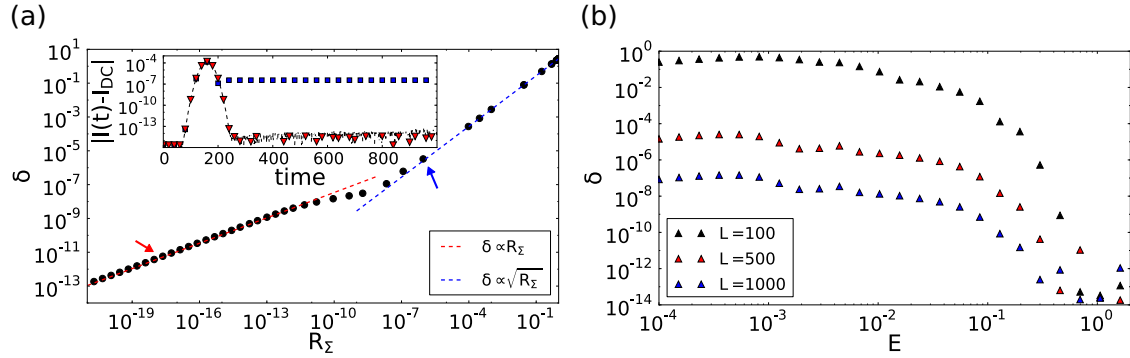


FIG. 4. Scaling of the error δ in the time-dependent simulation with respect to (a) the dc reflection probability R_Σ and (b) the particle injection energy E . A monomial complex absorbing potential (CAP) with $n = 6$ was used. For (a) simulations were carried out at a single energy at the center of the band and the length of the absorbing region was varied. Dashed lines show fits to $\delta \propto R_\Sigma$ (blue) and $\delta \propto \sqrt{R_\Sigma}$ (red). Inset: Deviation of the probability current from equilibrium for different lengths of the absorbing region corresponding to the two points indicated by arrows in the main figure. The black dashed curve shows the reference calculation.

as one decreases the energy. Figure 4(b) indeed shows that the error increases as the energy is lowered. However, one finds that δ saturates at small energy. Furthermore, the saturated value decreases with L and can thus be controlled. This behavior comes from the structure of the wave function as shown in Eq. (13); even though one injects an electron at a definite energy inside the system, the energy of the outgoing wave is ill defined. The contribution to the wave function coming from spurious reflections takes the form

$$\delta \bar{\Psi}_{\alpha,E}(n,t) = \sum_{\alpha'} \int_0^\infty e^{-i(k'n+E't)} \xi_{\alpha'}(E') \times r_\Sigma(E') S_{\alpha'\alpha}(E',E) dE'. \quad (36)$$

The contribution spreads over an energy window E_{pulse} which characterizes the inelastic scattering matrix $S_{\alpha'\alpha}(E',E)$. $S_{\alpha'\alpha}(E',E)$ typically decays on an energy scale of the order of $E_{\text{pulse}} = \hbar/\tau_{\text{pulse}}$ (see Fig. 10 of Ref. [21] for an example). For the voltage pulse considered here (which sends one electron through the system), τ_{pulse} is essentially the duration of the pulse. The consequence is that the reflection r_Σ is averaged over an energy window of width E_{pulse} , which blurs the $E = 0$ behavior of r_Σ :

$$\delta \approx \langle r_\Sigma(E) \rangle_{E < E_{\text{pulse}}} \approx r_\Sigma(E_{\text{pulse}}). \quad (37)$$

We conclude that the error can always be made arbitrarily small, irrespective of the duration of the simulation. A slight drawback is that for a given imaginary potential, the precision of the calculation can depend on the actual physics taking place inside the central system (which sets E_{pulse}) if one injects electrons with energies close to the band edges of the leads.

C. A general algorithm

We now discuss how to turn the above results into a practical scheme to perform numerical calculations in a robust way. Since we cannot guarantee the error for a given shape of the imaginary potential (we have seen above that it might depend on the physics of the central region), we first need to design an algorithm for an on-fly calculation of an error estimate (without the reference calculation used above). This can be done as follows for a small additional computational cost. In

the integration of the Schrödinger equation, one separates the wave function in the central region $\bar{\psi}_0$ and in the leads $\bar{\psi}_1$ (let us suppose that there is only one lead for simplicity). The equations to be integrated take the block form,

$$i \partial_t \bar{\psi}_0 = H_{00}(t) \bar{\psi}_0 + H_{01} \bar{\psi}_1 + S_0(t), \quad (38)$$

$$i \partial_t \bar{\psi}_1 = H_{11}(\Sigma) \bar{\psi}_1 + H_{10} \bar{\psi}_0, \quad (39)$$

where $S_0(t)$ is the source term present in the central region and the imaginary potential is included in H_{11} . One then introduces a second ‘‘copy’’ of the lead wave function $\bar{\psi}'_1$ that uses a different imaginary potential $H_{11}(\Sigma')$. The equations of motion for this ‘‘copy’’ are

$$i \partial_t \bar{\psi}'_1 = H_{11}(\Sigma') \bar{\psi}'_1 + H_{10} \bar{\psi}_0. \quad (40)$$

One then keeps track of both $\bar{\psi}_1$ and $\bar{\psi}'_1$ simultaneously, although only $\bar{\psi}_1$ will affect the dynamics of $\bar{\psi}_0$. The trick is to design $\Sigma'(n) = \Sigma(n - M)$, i.e., to insert M extra lead layers before the imaginary potential, and to monitor the difference between $\bar{\psi}'_1$ and $\bar{\psi}_1$ in the lead cell adjacent to the central region, $\delta \bar{\psi}_1 = \bar{\psi}_1 - \bar{\psi}'_1$. Spurious reflections from the presence of Σ will arrive at the boundary of the central region for $\bar{\psi}_1$ before $\bar{\psi}'_1$, as the latter has M extra lead layers. This delay in the arrival of the spurious reflections will give rise to a finite $\delta \bar{\psi}_1$. Note that $\delta \bar{\psi}_1$ will remain 0 in the case that there are no spurious reflections. $\delta \bar{\psi}_1$ can thus be used as an error estimate for the wave function in the lead.

In the worst case scenario this scheme will increase the computational cost by a factor of 2 (when the absorbing region represents the largest part of the system). It is worth noting, however, that without an error estimate for the spurious reflections one would have to check for convergence of results by performing several simulations with different values of L , the absorbing region length.

The remaining task is to choose the parameters A and L for a given shape of the imaginary potential. Ideally, we would choose L as small as possible so as to minimize the extra computational effort while requiring that $|\delta \bar{\psi}_1|$ remain smaller than a fixed maximum error δ_{max} . Given δ_{max} it is easy to choose A such that the first term in Eq. (34) is not a limitation.

By noting that $e^{-Ak/E} < e^{-A/(aB)}$ (B is the lead bandwidth and a is the discretization step) we see that it is sufficient to choose A such that $e^{-A/(aB)} < \delta_{\max}$ for the absorption process not to be the limiting factor of the precision. Next, one needs to choose L large enough to enforce $|\delta\tilde{\psi}_\uparrow| < \delta_{\max}$. In practice, we found that a few hundred (up to a thousand) lead cells are almost always sufficient for the physics we have studied so far, for typical $\delta_{\max} \sim 10^{-5}$.

Let us end with a last point of practical importance. We have seen that the major contribution to spurious reflection comes from a narrow region around the band edge of the lead. The wave functions associated with these energies propagate *extremely* slowly into the absorbing region due to the vanishing velocity at the band edge. Unless one is interested in extremely long simulation times, we can take advantage of this by placing a small number of lead layers before the imaginary potential. The slow-moving waves will induce spurious reflections, but will take a long time to traverse this buffer layer due to their small group velocity. Meanwhile, the absorbing region does not have to be made as long, as it does not have to absorb waves of vanishingly small energy.

V. VOLTAGE PULSES IN LONG JOSEPHSON JUNCTIONS

We are now in possession of a robust algorithm to simulate time-dependent open systems. Compared with our own previous approach, the computing time is now $O(Nt_{\max})$. This algorithm allows us to treat cases where very small energies (hence large times) come into play. We now turn to a specific application concerning superconducting-normal-superconducting (SNS) Josephson junctions where the large separation of scales $E_{\text{th}} \ll \Delta_0 \ll E_F$ (E_{th} : Thouless energy; Δ_0 : superconducting gap; E_F : Fermi energy) makes a linear-scaling algorithm very welcome. An interesting aspect of superconductivity is that the problem is intrinsically time dependent *even in dc* as soon as there are voltage differences across the superconductors (as evidenced by the ac Josephson effect, which transforms a dc voltage into an ac current). We emphasize that the algorithm is in no way limited to superconductivity and refer to the Introduction for other applications (such as quantum Hall effect, graphene, etc.).

In the following, we will focus on three physical effects. First, we will recover the known physics of Josephson junctions: the multiple Andreev reflection (MAR) phenomena and the ac Josephson effect. Second, we will discuss the relaxation of a SNS junction after an abrupt rise of the applied potential, showing how MAR comes into play in the relaxation rate. Third, we will study an interesting phenomenon, the propagation of a voltage pulse through a Josephson junction [39].

A. Minimum microscopic model for a SNS junction

We consider voltage-biased Josephson junctions. In this setup we have two infinite superconducting reservoirs coupled by a normal region of length L . We shall treat the problem using a 1D Bogoliubov–de Gennes Hamiltonian [40],

$$\hat{H} = \int_{-\infty}^{\infty} \hat{\Psi}^\dagger(x) \begin{pmatrix} \frac{p^2}{2m} - \mu(x,t) & \Delta(x,t) \\ \Delta(x,t)^* & \mu(x,t) - \frac{p^2}{2m} \end{pmatrix} \hat{\Psi}(x) dx, \quad (41)$$

where $p = -i\hbar\frac{\partial}{\partial x}$, $\hat{\Psi}(x) = (\hat{\psi}_\uparrow(x), \hat{\psi}_\downarrow(x))^T$, and $\hat{\psi}_\uparrow(x)$ is an operator that annihilates an electron at position x in a spin up state. $\Delta(x,t)$ is the superconducting order parameter, which reads

$$\Delta(x,t) = \begin{cases} \Delta_0 & \text{for } x > L, \\ 0 & \text{for } 0 \leq x \leq L, \\ \Delta_0 \exp[-2i\phi(t)] & \text{for } x < 0, \end{cases} \quad (42)$$

with $\phi(t) = (e/\hbar) \int_0^t V_b(\tau) d\tau$ and $V_b(t)$ is the voltage bias applied to the left superconductor (which is 0 before $t = 0$). Likewise, the electrochemical potential $\mu(x,t)$ reads

$$\mu(x,t) = \begin{cases} E_F + V_b(t) & \text{for } x < 0, \\ E_F + U(x) & \text{for } 0 \leq x \leq L, \\ E_F & \text{for } x > L, \end{cases} \quad (43)$$

where E_F is the Fermi energy and $U(x)$ a potential barrier. We only consider a single spin sector; our model is spin independent so the two spin sectors give degenerate solutions.

In order to put Eq. (41) into a form where we can apply the algorithm developed above, we first apply a gauge transformation

$$\hat{\Psi}'(x) = [\Theta(x) + \Theta(-x) \exp[i\phi(t)\tau_z]] \hat{\Psi}(x), \quad (44)$$

where $\tau_{\{x,y,z\}}$ are Pauli matrices and $\Theta(x)$ is the Heaviside function. This transformation brings all the time dependence for $x < 0$ into a time dependence in the momentum term at $x = 0$, the boundary between the left superconductor and the normal region. In this gauge both superconductors are at equilibrium. We next discretize onto a lattice with spacing a , using a central difference approximation for the second spatial derivative, $\partial^2\Psi/\partial y^2 \approx [\Psi(y+a) + \Psi(y-a) - 2\Psi(y)]/a^2$, to obtain a tight-binding model

$$\hat{H}_{\text{tb}} = \sum_{i,j=-\infty}^{\infty} \hat{\mathbf{c}}_i^\dagger \mathbf{H}_{i,j}(t) \hat{\mathbf{c}}_j, \quad (45)$$

with the matrices $\mathbf{H}_{i,j}(t)$ being nonzero only for diagonal and nearest-neighbor matrix elements,

$$\mathbf{H}_{j,j}(t) = \left[\frac{\hbar^2}{ma^2} - E_F + U_j \right] \tau_z + \Delta_0(\theta_{0,j} + \theta_{j,L}) \tau_x, \quad (46)$$

$$\mathbf{H}_{j,j+1}(t) = \frac{-\hbar^2}{2ma^2} \tau_z \exp[i\phi(t)\delta_{j,0}\tau_z], \quad (47)$$

$$\mathbf{H}_{j,j-1}(t) = [\mathbf{H}_{j,j+1}(t)]^\dagger, \quad (48)$$

where $\hat{\mathbf{c}}_j \equiv \hat{\Psi}(ja) = (\hat{\psi}_\uparrow(ja), \hat{\psi}_\downarrow(ja))^T$ (and $\hat{\mathbf{c}}_j^\dagger$, its Hermitian conjugate) are vectors of creation (annihilation) operators at site j . $\delta_{i,j}$ is the Kronecker delta and $\theta_{i,j}$ is a discrete Heaviside function, defined as 1 if $i > j$ and 0 otherwise. U_i is the potential barrier.

This model can be readily solved numerically using the above-developed technique. In practice, we use a 4(5) order embedded Runge-Kutta method [41] with an adaptive time step to solve the time-dependent Schrödinger equation. Although using a fully explicit, nonunitary integrator will in principle induce errors in the result, we check the magnitude of such errors using the continuity equation for the quasiparticle current/density. In practice, we found that there is a significant advantage in terms of speed (for a given accuracy) to using such

methods. For the energy integration we subdivide the energy interval into subintervals and use a 15(7) point Gauss-Kronrod embedded scheme [42] on each subinterval. The subintervals are chosen manually based on previous simulation runs, and the error in the result is verified to be below a certain threshold using a standard error estimate for Gauss-Kronrod schemes [42].

B. Multiple Andreev reflection and ac Josephson effect

Let us now apply our numerical technique and discuss the physics of a voltage-biased Josephson junction. There are two very different regimes to discuss: At low voltage one observes the ac Josephson effect, while at higher voltage one observes multiple Andreev reflections (MARs). Both effects are closely related, as the Josephson effect corresponds to the limit of an infinite number of Andreev reflections, yet they are usually calculated with different techniques. Indeed, one of the challenges of such a simulation is that to access small bias voltages V_b one needs to go to very long times $\propto \hbar/V_b$. For this problem the source-sink algorithm thus has a distinct advantage over previous methods due to its linear scaling with simulation time.

In this section, we concentrate on a short junction and add a potential barrier $U(x)$ that allows us to tune the transmission probability D of the normal part of the junction from insulating $D \ll 1$ to ballistic $D = 1$. To obtain a current-voltage characteristic for the junction we perform a separate simulation for each value of voltage required. For a given simulation (voltage value) we use the following protocol. At $t = 0$ the voltage of the left superconductor is raised smoothly, $V_b(t) = (V_0/2)[1 - \cos(\pi t/T)]$, until $t = T$, when V_b is held at a value V_0 (we used $T = 50 \hbar/\Delta$). The system relaxes to a steady state and we can obtain the current using Eq. (5). The dc current can then be obtained by taking an average over one period of the fully time-dependent current after the system has reached a steady state.

Let us start with the ac Josephson effect. At equilibrium, the ground state energy $E(\phi)$ of the junction depends on the phase difference ϕ between the order parameters of the two superconductors. The corresponding supercurrent is given by

$$I = (2e/\hbar)\partial E/\partial\phi \propto \cos\phi. \quad (49)$$

When a small bias is applied to the junction, ϕ increases linearly in time $\phi(t) = 2eV_b t/\hbar$ and one observes the ac Josephson effect at frequency $2eV_b/\hbar$. This is perhaps the most striking manifestation of superconductivity; a dc bias leads to an ac effect. Figure 5 shows a numerical calculation of the current as a function of time together with the adiabatic prediction discussed above [the dispersion relation $E(\phi)$ was calculated from the equilibrium junction and differentiated numerically]. We see a perfect agreement at low bias, indicating that our technique can reach the adiabatic limit. Upon increasing the bias, one leaves the adiabatic limit and the corresponding prediction becomes less accurate.

Indeed, as one increases the bias, a dc component starts to appear in the current. This is best understood starting from large bias. For $V_b > 2\Delta_0/e$, the charges can flow directly from the left “valence” band of the superconductor to the right “conduction” band (using the semiconductor

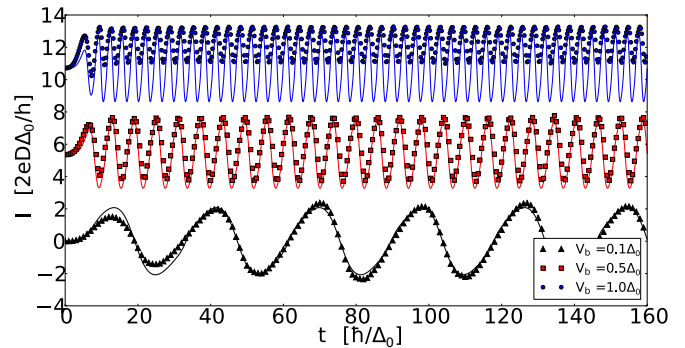


FIG. 5. The ac Josephson effect. The different curves show the calculated current as a function of time for different bias voltages across a short junction with a transmission of 0.7. The solid curves and symbols show the theoretical and numerical results, respectively. The curves have been vertically offset for clarity.

terminology). As one lowers the bias, this direct process is no longer possible and at least one Andreev reflection takes place on the right superconductor. As one further lowers the bias, more and more Andreev reflections are needed and one observes kink in the I - V characteristics at values $V_b > 2\Delta_0/Ne$ with $N = 1, 2, 3, \dots$. The Fourier components of the MAR current have been previously calculated using a Floquet approach [43,44], and are routinely observed experimentally (see, for instance, Ref. [45]). More recently, some results were obtained with techniques working in the time domain [39,46]. The calculations given below follow a similar line. However, the favorable scaling of our algorithm allows us, without resorting to approximations such as the wide band limit, to reach unprecedented large system sizes and/or simulation times. Let us start by recovering the MAR physics using a microscopic model for the junction. Figure 6 compares the current-voltage characteristics of such a junction calculated in Ref. [43] with a simulation using the source-sink algorithm for different values of the transmission (D) of the junction. We see a very good quantitative agreement with these previous results.

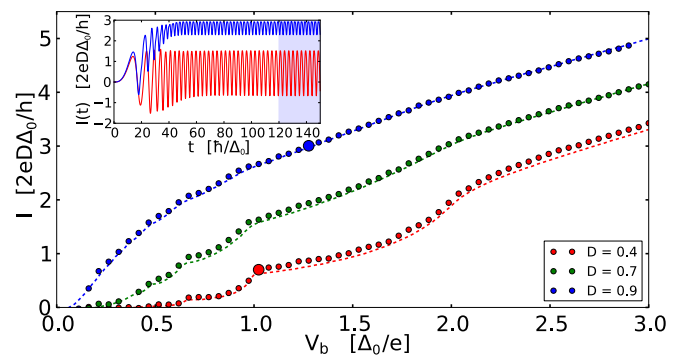


FIG. 6. dc current-voltage curve showing the analytical results from Ref. [43] (dashed line) and the source-sink numerical calculation (points) for different values of the transmission (D) of the insulating link. Inset: Time series corresponding to the enlarged points in the main figure, showing a typical averaging window over which the dc current was calculated. For these simulations we used $\Delta = 0.02\gamma$, with γ the hopping parameter.

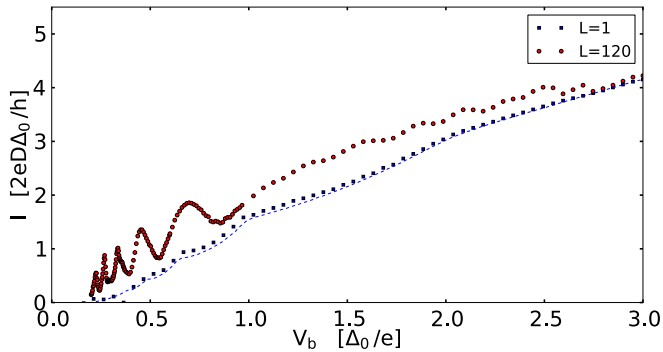


FIG. 7. Comparison of the current-voltage characteristics for a short junction (one site in the normal region) and a long junction (120 sites in the normal region). Both the junctions have a transmission of 0.7. For these simulations we used $\Delta = 0.02\gamma$, with γ the hopping parameter.

Using the source-sink algorithm we can go beyond the limitations of an analytical approach for little extra overhead. We can, for example, explore the behavior of a long Josephson junction under voltage bias. Figure 7 compares the current-voltage characteristics of a long junction with the short junction studied previously. We clearly see that the long junction has more subgap features, which can be attributed to the larger number of Andreev states below the gap. We see that numerics has an advantage over analytical approaches in this regard, in that it is relatively cheap to explore new regions of parameter space or in crossover regions between tractable limits (e.g., short junction versus long junction).

C. Relaxation of Andreev bound states

An important difference of Josephson junctions with respect to other nanoelectronics systems is the presence of (so-called Andreev) bound states. Since Andreev states have their energies inside the superconducting gap, there is no continuum band with which they can hybridize so that they have an infinite lifetime. These states must be added explicitly in Eq. (5) and the definitions of the Green's function (see Sec. IV of Ref. [29] for a discussion). As the Andreev states carry the Josephson current, their role is particularly important and they cannot be ignored. This is in contrast to many nonsuperconducting systems where the bound states do not contribute to transport.

Andreev states give us another opportunity to study MAR physics. Suppose that we abruptly raise the voltage bias at $t = 0$, thereby placing the system in a nonequilibrium state. Just after the voltage rise, a given wave function can be decomposed on the eigenbasis of the equilibrium SNS junction,

$$\Psi = \sum_{\alpha} \int dE c_{\alpha}(E) \Psi_{\alpha E}^{\text{st}} + \sum_n c_n \Psi_n^{\text{st}}, \quad (50)$$

where $c_{\alpha}(E)$ and c_n are, respectively, the projection of the wave function on the scattering states ($\Psi_{\alpha E}^{\text{st}}$) and the bound states (Ψ_n^{st}). It is important to realize that in the absence of bias voltage, the bound state part of the wave function will *never* relax (within the above model) as the Andreev states are true bound states with energy E_n : The second part of the

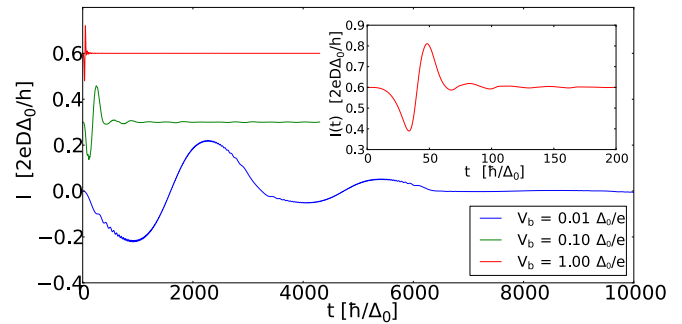


FIG. 8. Current contribution from the (Andreev) bound states at different bias voltages. The curves have been offset for clarity. The inset shows a zoom of the curve for $V_b = \Delta/e$.

wave function will simply oscillate as $\sum_n c_n e^{-iE_n t} \Psi_n^{\text{st}}$ forever. However, the presence of the bias voltage allows the energy to change by eV in between two Andreev reflections so that after $N \approx \Delta_0/(eV_b)$ reflections, one can reach energies outside the gap and the wave function can relax. Denoting $\tau_P = L/v_F$ the time of flight between two Andreev reflections, we expect the relaxation time τ_R of the system to behave as $\tau_R \propto N\tau_F = L\Delta_0/(v_F e V_b)$.

Figure 8 shows the contribution of the Andreev bound states to the current as a function of time for three values of the bias voltage. We indeed see that the current carried by the bound states dies away with time in the presence of a finite bias. Although we did not try to define τ_R precisely, we clearly see that dividing V_b by a factor of 10 leads to a tenfold increase in the relaxation time, establishing the relation $\tau_R \propto 1/V_b$, which originates from the MAR assisted relaxation process.

From a numerical perspective, we note that these simulations are taken to extremely long times, 10^5 in units of the inverse hopping parameter, γ ($= \hbar^2/2m^*a^2$), of the model (we chose $\Delta = 0.1\gamma$ for the bound state calculations and $\Delta = 0.02\gamma$ for the calculations of the MAR I - V curve). This calculation clearly necessitates the source-sink algorithm; we used an imaginary absorbing potential of order $n = 6$ with 1000 lead cells forming the absorbing layer.

D. Propagation of a voltage pulse through a Josephson junction

A natural consequence of the above discussion is that if one sends a fast voltage *pulse* through the system (i.e., the final bias voltage vanishes instead of having a finite value), then the corresponding bound state contribution will not relax and will oscillate forever (within the assumptions of our model).

Let us study the corresponding protocol. We consider a perfectly transparent junction with a finite width, and apply a Gaussian voltage pulse of duration τ_P on the left superconducting contact. The junction has a length L such that the time of flight is $\tau_F = L/v_F$. We consider a “long” junction, such that $\Delta_0\tau_F/\hbar \gg 1$. We further consider fast pulses with $\tau_F/\tau_P \gg 1$ ($\tau_F/\tau_P \sim 5$ in our case). The case of slow pulses is trivial as the physics is essentially given by the adiabatic limit. The physics of fast pulses is simple yet rather interesting. The pulse generates an electronlike excitation that propagates through the system until it reaches the right superconductor. There, it is Andreev reflected as a

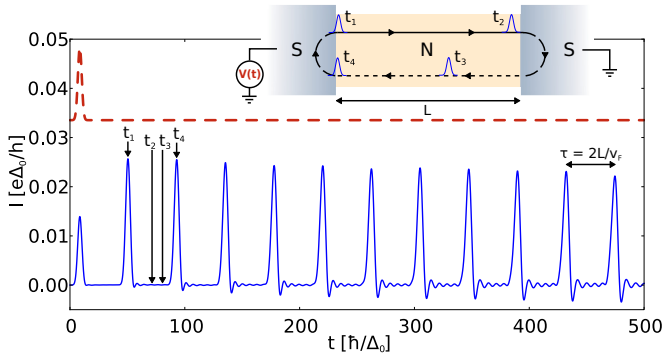


FIG. 9. Current (blue solid line) and voltage (red dashed line, offset for clarity) at the left superconducting-normal contact as a function of time. Inset: Propagation of the charge pulse through the junction at different times (t_1, t_2, t_3, t_4) and the corresponding times indicated on the main plot.

holelike excitation and a Cooper pair is generated in the right electrode. The excitation now propagates backward towards the left superconducting electrode where it is Andreev reflected a second time (and a Cooper pair is absorbed from the electrode). The excitation then continues its propagation again to the right. Within the above model, nothing stops this process and the excitation continues to oscillate back and forth forever. This is rather appealing: One sends a short voltage pulse and gets an oscillating current at frequency $1/(2\tau_F)$. Beyond the current model, the relaxation time of the system will be given by the fluctuations of the voltage due to the electromagnetic environment and we anticipate a relaxation of the current on a scale given by the corresponding RC time.

Figure 9 shows a numerical simulation of the propagation of a voltage pulse as discussed above. Despite the fact that there is only a single voltage pulse at the start, we see pulses of current every $2\tau_F$. We do not observe any quasiparticle current in the superconducting lead; this (super)current is purely associated with the Andreev reflection process described above.

We can go a little bit further and look at the structure of the bound states that carry the supercurrent. They are given by the stationary condition [25,47,48],

$$r_A^2 e^{2iE\tau_F/\hbar} e^{i\phi} = 1, \quad (51)$$

where the left-hand superconductor is at a phase bias ϕ compared to the right-hand one and $r_A = E/\Delta_0 - i\sqrt{1 - (E/\Delta_0)^2}$ is the Andreev reflection amplitude for a particle incident on the superconductor at energy E . The paths contributing to this amplitude are sketched in Fig. 10(a). A similar expression exists for the reversed paths where the sign of ϕ is flipped; this is sketched in Fig. 10(b). For $E < \Delta_0$ we have $r_A = e^{-i \arccos(E/\Delta_0)}$, and we can rewrite this condition as

$$-2 \arccos(E/\Delta_0) + \frac{2E\tau_F}{\hbar} \pm \phi = 2\pi m, \quad m \in \mathbb{Z}. \quad (52)$$

In the long junction limit ($\Delta_0 \gg \hbar/\tau_F$) close to zero energy, this simplifies to

$$E = \frac{\hbar}{2\tau_F} \left[m + \frac{1}{2} \mp \frac{\phi}{2\pi} \right], \quad (53)$$

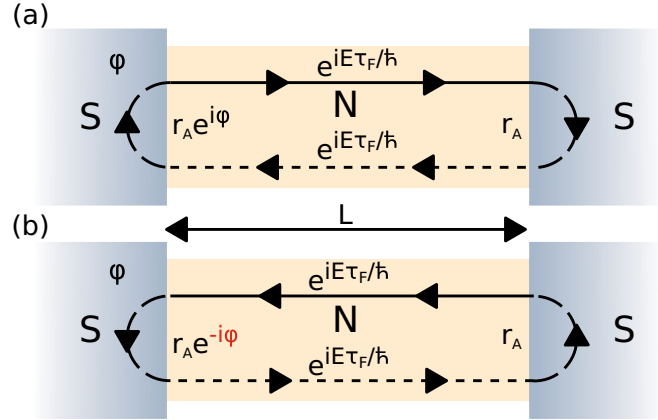


FIG. 10. Sketches of the two classes of paths that can result in bound states. The solid lines correspond to an electronlike excitation, and the dashed line to a holelike one. Andreev reflection at the normal-superconductor interface converts an electronlike excitation to a holelike one. Each sketch actually represents a set of paths with 1, 2, 3, ... pairs of Andreev reflections.

which corresponds to two sets of equidistant energies separated by $\hbar/(2\tau_F)$, one set that has energy increasing with ϕ , and the other decreasing with ϕ . Each of these sets corresponds to ballistic propagation in the continuum limit $\tau_P \ll \tau_F$. The numerical spectrum, which is shown in Fig. 11, adheres to the above-derived result except near the degeneracy points. The degeneracies are lifted due to the finite ratio Δ_0/E_F used in the numerical calculation, which induces a finite normal reflection at the normal-superconducting interfaces. The two insets of Fig. 11 show two time-dependent simulations at two different values of the superconducting phase difference *after* the pulse, $\phi = \phi(t = \infty)$. We see that when the two sets of bound states are very close in energy the output current beats with a frequency that is given by the level spacing. For

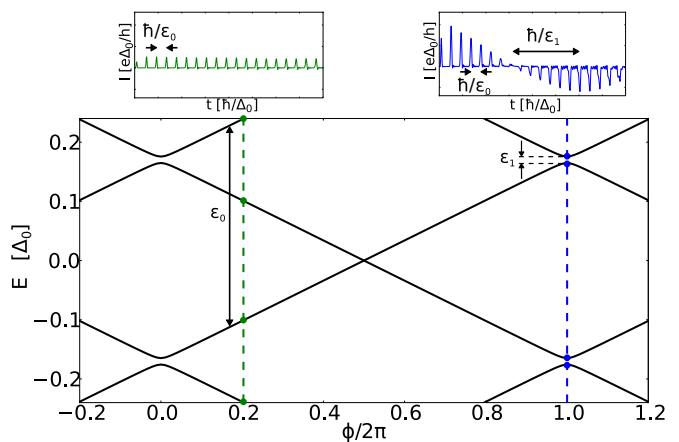


FIG. 11. A section around $E = 0$ of the bound state spectrum after the passage of a pulse as a function of the phase ϕ picked up from the pulse. The vertical dashed lines highlight the bound state energies for two values of ϕ . The current flowing through the junction as a function of time is shown in the traces above the main figure. The spectrum was calculated numerically by diagonalizing the Hamiltonian of the system projected onto a large, finite region around the junction

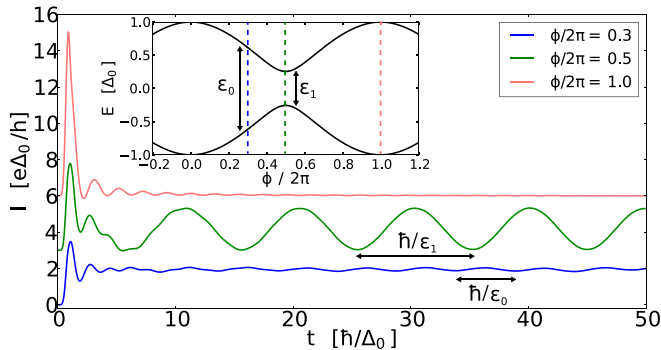


FIG. 12. Current traces as a function of time for three different voltage pulses applied to a short Josephson junction with a transparency of 0.9. The curves have been offset for clarity. Each pulse has a full width at half maximum of $0.4 \hbar/\Delta_0$, and the pulses are of different heights. This gives a different phase bias ϕ across the junction after the pulse has completed. Inset: The bound state spectrum for the junction as a function of the phase bias; the phases accumulated by the three pulses are indicated by colored lines.

well-spaced bound states this frequency is so high that it has no visible effect on the current trace.

The above effect is intriguing, but unfortunately long ballistic Josephson junctions are difficult to realize experimentally (with the exception perhaps of carbon nanotubes). In diffusive junctions there will be a distribution of times of flight which will wash out the above effect. An alternative is to consider the limit of short junctions, which have been studied extensively experimentally with atomic contacts (break junctions) [45]. We shall, therefore, now explore the effect of a voltage pulse applied to a short Josephson junction. We do not expect to be able to see a train of well-resolved peaks of current, as in the long junction case, because the time of flight of the short junction is much shorter than the typical pulse duration. We do, however, expect to see the effect that gives rise to the “beating” in Fig. 11, as this is governed only by the energy difference between the Andreev bound states in the junction. Figure 12 shows the current passing through a short junction when voltage pulses of varying heights are applied. We see an initial transient part followed by an oscillatory part that continues indefinitely. Initially, all the states up to $E = 0$ are filled (Pauli principle). The pulse excites some quasiparticles into states at $E > 0$ and also shifts the phase bias across the junction so that we are at a different place in the phase-energy plot than we were before the pulse (indicated by dashed lines in the inset to Fig. 12). Any quasiparticles in continuum states escape into the leads after some time ($\sim 20\hbar/\Delta$ in Fig. 12), however, the contribution in the Andreev bound states cannot escape. After we have reached a steady state we are essentially in a superposition of Andreev bound states at energy E and $-E$. These two contributions interfere with one another to give a current that *oscillates* in time at an angular frequency $2E/\hbar$. This effect is most strongly seen for $\phi = \pi$, as the Andreev levels have the smallest energy gap here. For $\phi = 2\pi$ the oscillations die away with time, as the Andreev levels hybridize with the continuum at this point. By tuning the energy gap between the Andreev levels after the pulse we are able to control the frequency of the current. We can tune the

energy gap by placing ourselves at different points in the phase-energy diagram (by sending in pulses of different heights), or by tuning the transparency of the junction to modify the phase-energy diagram itself. The above calculations have been performed in the absence of an electromagnetic environment. The closest experimental situation that would correspond to these calculations is a Josephson junction embedded in a superconducting ring where the voltage pulse is applied through a pulse of magnetic field through the ring and the signal detected through the magnetization generated by the oscillating circulating current. A simpler configuration would involve a superconducting quantum interference device (SQUID) where one of the two junctions is an atomic one and the other a regular large tunnel junction. In a SQUID setup, however, the effect of the electromagnetic environment would have to be properly included.

VI. CONCLUSION

We have developed an algorithm for simulating time-resolved quantum transport, which we dub “source-sink” due to the characteristic addition of both “source” and “sink” terms to the Schrödinger-like equations used. We demonstrated that the accuracy of the method can be tuned at the cost of increasing the runtime, and that for a given accuracy the algorithm scales linearly with the system size and the maximum time required. We confirmed the accuracy of the method by comparing our results for a Josephson junction at finite bias with analytical results from the literature. In its present form, the algorithm only applies to quadratic (i.e., noninteracting) Hamiltonians. The algorithm can be straightforwardly extended to deal with interactions at the mean field level. This would encompass Hartree and time-dependent density functional theory, but would also allow us to couple to other degrees of freedom, such as the Landau-Lifshitz-Gilbert equation in a magnetic system or the circuit electromagnetic environment for the Josephson junction considered here. The cost for such an extension is that the different Schrödinger equations for the different energies would be coupled by the mean field and therefore cannot be solved independently. This complicates the (parallel) implementation of the algorithm, and is the subject of current work. In the same spirit, one could also include some quantum fluctuations through the addition of a noise term in the Schrödinger-like equation of our method. Correlations beyond mean field, however, are beyond the scope of this approach in its present form.

We then studied the effect of a single voltage pulse on a (long or short) Josephson junction. We found that a single voltage pulse results in a periodic resultant supercurrent. The (rightly) controversial yet appealing concept of time crystal was recently put forward [49]. In analogy with a regular crystal where translational spatial symmetry is spontaneously broken, a time crystal would spontaneously break translational time symmetry. While the above effect is not a time crystal (the system in the normal part is not in its ground state), it might be as close as one can get; the superconducting ring remains in its ground state, yet a time-dependent current flows through it.

In contrast to other universal effects associated with Josephson physics, the period is given here by the normal part of the

device. In the absence of an electromagnetic environment, the periodic current continues forever. A precise calculation of the effect of the dissipative electromagnetic environment to damp the oscillating current is left for future work.

ACKNOWLEDGMENTS

This work is funded by the ERC consolidator grant MesoQMC.

-
- [1] J. Dubois, T. Jullien, F. Portier, P. Roche, A. Cavanna, Y. Jin, W. Wegscheider, P. Roulleau, and D. C. Glatli, *Nature (London)* **502**, 659 (2013).
- [2] G. Fève, A. Mahé, J.-M. Berroir, T. Kontos, B. Plaçais, D. C. Glatli, A. Cavanna, B. Etienne, and Y. Jin, *Science* **316**, 1169 (2007).
- [3] R. C. Ashoori, H. L. Stormer, L. N. Pfeiffer, K. W. Baldwin, and K. West, *Phys. Rev. B* **45**, 3894 (1992).
- [4] H. Kamata, T. Ota, K. Muraki, and T. Fujisawa, *Phys. Rev. B* **81**, 085329 (2010).
- [5] N. Kumada, H. Kamata, and T. Fujisawa, *Phys. Rev. B* **84**, 045314 (2011).
- [6] Z. Zhong, N. M. Gabor, J. E. Sharping, A. L. Gaeta, and P. L. McEuen, *Nat. Nanotechnol.* **3**, 201 (2008).
- [7] N. S. Wingreen, A.-P. Jauho, and Y. Meir, *Phys. Rev. B* **48**, 8487 (1993).
- [8] A.-P. Jauho, N. S. Wingreen, and Y. Meir, *Phys. Rev. B* **50**, 5528 (1994).
- [9] R. Tuovinen, E. Perfetto, G. Stefanucci, and R. van Leeuwen, *Phys. Rev. B* **89**, 085131 (2014).
- [10] M. Ridley, A. MacKinnon, and L. Kantorovich, *Phys. Rev. B* **91**, 125433 (2015).
- [11] K. T. Cheung, B. Fu, Z. Yu, and J. Wang, *arXiv:1602.01638*.
- [12] V. Moldoveanu, V. Gudmundsson, and A. Manolescu, *Phys. Rev. B* **76**, 085330 (2007).
- [13] A. Prociuk and B. D. Dunietz, *Phys. Rev. B* **78**, 165112 (2008).
- [14] A. Croy and U. Saalman, *Phys. Rev. B* **80**, 245311 (2009).
- [15] L. Zhang, Y. Xing, and J. Wang, *Phys. Rev. B* **86**, 155438 (2012).
- [16] Y. Zhang, S. Chen, and G. H. Chen, *Phys. Rev. B* **87**, 085110 (2013).
- [17] S. Kurth, G. Stefanucci, C.-O. Almbladh, A. Rubio, and E. K. U. Gross, *Phys. Rev. B* **72**, 035308 (2005).
- [18] P. Bokes, F. Corsetti, and R. W. Godby, *Phys. Rev. Lett.* **101**, 046402 (2008).
- [19] G. Stefanucci, S. Kurth, A. Rubio, and E. K. U. Gross, *Phys. Rev. B* **77**, 075339 (2008).
- [20] Z. Zhou and S.-I. Chu, *Europhys. Lett.* **88**, 17008 (2009).
- [21] B. Gaury, J. Weston, M. Santin, M. Houzet, C. Groth, and X. Waintal, *Phys. Rep.* **534**, 1 (2014).
- [22] B. Gaury and X. Waintal, *Nat. Commun.* **5**, 3844 (2014).
- [23] B. Gaury, J. Weston, and X. Waintal, *Nat. Commun.* **6**, 6524 (2015).
- [24] B. Gaury, J. Weston, and X. Waintal, *Phys. Rev. B* **90**, 161305 (2014).
- [25] J. Weston, B. Gaury, and X. Waintal, *Phys. Rev. B* **92**, 020513 (2015).
- [26] M. Fruchart, P. Delplace, J. Weston, X. Waintal, and D. Carpentier, *Physica E*, **75** 287 (2016).
- [27] B. Gaury and X. Waintal, *Physica E* **75**, 72 (2016).
- [28] C. W. Groth, M. Wimmer, A. R. Akhmerov, and X. Waintal, *New J. Phys.* **16**, 063065 (2014).
- [29] R. E. V. Profumo, C. Groth, L. Messio, O. Parcollet, and X. Waintal, *Phys. Rev. B* **91**, 245154 (2015).
- [30] X. Antoine, A. Arnold, C. Besse, M. Ehrhardt, and A. Schädle, *Commun. Comput. Phys.* **4**, 729 (2008).
- [31] J. Muga, J. Palao, B. Navarro, and I. Egusquiza, *Phys. Rep.* **395**, 357 (2004).
- [32] O. Shemer, D. Brisker, and N. Moiseyev, *Phys. Rev. A* **71**, 032716 (2005).
- [33] U. V. Riss and H.-D. Meyer, *J. Phys. B* **31**, 2279 (1998).
- [34] U. V. Riss and H.-D. Meyer, *J. Phys. B* **28**, 1475 (1995).
- [35] D. J. Kalita and A. K. Gupta, *J. Chem. Phys.* **134**, 094301 (2011).
- [36] J.-Y. Ge and J. Z. H. Zhang, *J. Chem. Phys.* **108**, 1429 (1998).
- [37] R. Baer, T. Seideman, S. Ilani, and D. Neuhauser, *J. Chem. Phys.* **120**, 3387 (2004).
- [38] L. Zhang, J. Chen, and J. Wang, *Phys. Rev. B* **87**, 205401 (2013).
- [39] G. Stefanucci, E. Perfetto, and M. Cini, *Phys. Rev. B* **81**, 115446 (2010).
- [40] P. G. de Gennes, *Superconductivity of Metals and Alloys* (Benjamin, New York, 1966).
- [41] E. Fehlberg, *Computing* **6**, 61 (1970).
- [42] R. Piessens, *Quadpack: A Subroutine Package For Automatic Integration*, Springer Series in Computational Mathematics (Springer, Berlin, 1983).
- [43] D. Averin and A. Bardas, *Phys. Rev. Lett.* **75**, 1831 (1995).
- [44] J. C. Cuevas, A. Martín-Rodero, and A. Levy Yeyati, *Phys. Rev. B* **54**, 7366 (1996).
- [45] E. Scheer, P. Joyez, D. Esteve, C. Urbina, and M. H. Devoret, *Phys. Rev. Lett.* **78**, 3535 (1997).
- [46] E. Perfetto, G. Stefanucci, and M. Cini, *Phys. Rev. B* **80**, 205408 (2009).
- [47] S. Mi, D. I. Pikulin, M. Wimmer, and C. W. J. Beenakker, *Phys. Rev. B* **87**, 241405 (2013).
- [48] C. Beenakker, in *Transport Phenomena in Mesoscopic Systems*, edited by H. Fukuyama and T. Ando, Springer Series in Solid-State Sciences Vol. 109 (Springer, Berlin, 1992), pp. 235–253.
- [49] F. Wilczek, *Phys. Rev. Lett.* **109**, 160401 (2012).